Rheol Acta 37:307–327 (1998)

ORIGINAL CONTRIBUTION

Mark T. Arigo
Gareth H. McKinley

An experimental investigation of negative wakes behind spheres settling in a shear-thinning viscoelastic fluid

Received: 10 November 1997
Accepted: 1 May 1998

M.T. Arigo
Division of Engineering and Applied Sciences
Harvard University
Cambridge, Massachusetts 02138, USA

G.H. McKinley (✉)
Department of Mechanical Engineering
Massachusetts Institute of Technology
Cambridge, Massachusetts 02139, USA

Abstract We present detailed experimental results examining "negative wakes" behind spheres settling along the centerline of a tube containing a viscoelastic aqueous polyacrylamide solution. Negative wakes are found for all Deborah numbers ($2.43 \le De(\dot{\gamma}) \le 8.75$) and sphere-to-tube aspect ratios ($0.060 \le a/R \le 0.396$) examined. The wake structures are investigated using laser-Doppler velocimetry (LDV) to examine the centerline fluid velocity around the sphere and digital particle image velocimetry (DPIV) for full-field velocity profiles. For a fixed aspect ratio, the magnitude of the most negative velocity, U_{min}, in the wake is seen to increase with increasing *De*. Additionally, as the Deborah number becomes larger, the location of this minimum velocity shifts farther downstream. When normalized with the sphere radius and the steady state velocity of the sphere, the axial velocity profiles become self-similar to the point of the minimum velocity. Beyond this point, the wake structure varies weakly with aspect ratio and *De*, and it extends more than 20 radii downstream. Inertial effects at high Reynolds numbers are observed to shift the entire negative wake farther downstream. Using DPIV to investigate the transient kinematic response of the fluid to the initial acceleration of the sphere from rest, it is seen that the wake develops from the nonlinear fluid response at large strains. Measurements of the transient uniaxial extensional viscosity of this weakly strain-hardening fluid using a filament stretching rheometer show that the existence of a negative wake is consistent with theoretical arguments based on the opposing roles of extensional stresses and shearing stresses in the wake of the sphere.

Key words Sphere – negative wake – viscoelastic – shear-thinning – strain-hardening

Introduction

As a benchmark problem for computational rheology and the evaluation of numerical codes, the sedimentation of a sphere in an elastic fluid has become one of the most studied problems in non-Newtonian fluid mechanics (see, e.g., Chhabra, 1992; Hassager, 1988; Walters and Tanner, 1992). In recent years, good agreement has been achieved in comparisons between experimental results and numerical computations using nonlinear, multimode constitutive equations for constant viscosity, elastic Boger fluids (see, e.g., Arigo et al., 1995; Rajagopalan et al., 1996). However, most concentrated polymeric solutions and melts have shear-thinning viscoelastic material properties. Arigo and McKinley (1997) have previously examined the transient response of a sphere accelerating from rest in a

RA 897

shear-thinning fluid, and we continue that experimental investigation by examining the steady-state kinematics of the flow that is established in the wake of a sphere sedimenting in the same fluid. In particular, we focus on the structure and development of a "negative wake," i.e., an additional recirculating region downstream of the sphere in which the fluid velocity is in the direction opposite to the motion of the sphere and the vorticity is reversed compared to the motion near the sphere.

When a sphere of radius a and density ρ_s settles in a Newtonian fluid of constant viscosity η_0 and density ρ_f, the development of the velocity field around the sphere and the steady state velocity of the sphere, U_s, are well understood. In the discussion that follows, we refer to a laboratory reference frame in which the sphere falls at a steady state velocity U_s and the fluid is quiescent at infinity. At low Reynolds numbers ($Re = \rho_f a U_s/\eta_0 \ll 1$), the fluid velocity is fore-aft symmetric and decays monotonically to zero with increasing distance from the sphere. Numerous researchers have documented experimentally and numerically the effects of perturbations to this flow, resulting in more complex wake structures downstream of the sphere. The most common example of such a perturbation is the high Reynolds number flow past a sphere confined in a cylindrical tube. For moderate Reynolds numbers, inertia acts to shift the fluid streamlines farther downstream. When the Reynolds number exceeds a critical value, $Re_{crit} \sim 15$, a steady, axisymmetric recirculating vortex develops in the wake behind the sphere in which the velocity along the centerline of the tube is greater than that of the sphere (e.g., photographs in van Dyke, 1982). This recirculating wake elongates with increasing Re, and eventually the stability of this structure breaks down beyond a second critical Reynolds number for $Re_{crit} > 65$ (Zheng et al., 1991; Tavener, 1994).

The wake structure downstream of a sphere settling in a constant viscosity, elastic "Boger" fluid at vanishing Reynolds numbers has often been qualitatively described as similar to the inertial shift seen in moderate Reynolds number flows of Newtonian fluids. However, in this case the effect is due to fluid elasticity and is characterized by the Deborah number $De = \lambda U_s/a$, where λ is a characteristic relaxation time of the polymer molecules. As a result of the high extensional viscosities of Boger fluids and the strong extensional flow in the wake of the sphere, the fluid velocity decays much slower than in the Newtonian case resulting in a wake structure that extends far downstream. However, this slow decay of the fluid velocity has been found to be monotonic and stable in all experimental studies (Bush, 1993; Arigo and McKinley, 1994; Arigo et al., 1995).

While the majority of experimental studies have concentrated on constant viscosity fluids, there have been few detailed investigations of the wake structure for shear-thinning viscoelastic fluids. Acharya et al. (1976) examined the flow behind spheres settling at high Reynolds numbers in an unbounded domain of shear-thinning, aqueous polymer solutions containing varying concentrations of polyacrylamide (PAA), polyethylene-oxide (PEO), or hydroxyethylcellulose (HEC). They describe flows in which elastic forces dominate and additional experiments in which inertia is the dominant factor. In the transition region between the two cases, they discovered a "dual wake" formation, i.e., an elastically-dominated region close to the sphere enveloped by an inertia-dominated region further away from the sphere.

In extensive investigations by Sigli and Coutanceau (1977), photographic flow visualization techniques were used to study the spatial kinematics of the viscoelastic wake structure. Their experiments were performed at low Reynolds numbers and low Deborah numbers in shear-thinning viscoelastic solutions containing moderate concentrations of PEO ($1\% \le c \le 2.5\%$). The photographs show the existence of a secondary recirculation region in the wake of the sphere. Immediately downstream of the sphere, the fluid in the wake moves in the same direction as the sphere, but, at greater distances, the flow reverses and moves away from the sphere. The authors also found that increasing the sphere-to-tube aspect ratio increases the elastic effect, whereas inertial effects act to dampen the elastic effects. Sigli and Coutanceau were also able to model this flow behavior assuming a constant viscosity Maxwell constitutive equation with simplified boundary conditions in which the velocity disturbance is confined within a spherical region of radius equal to the cylinder radius.

Hassager (1979) later termed this flow phenomenon a "negative wake" when he found the same type of recirculating region in the wakes behind bubbles rising in a shear-thinning, viscoelastic solution of 1% PAA in glycerol. Maalouf and Sigli (1984) have demonstrated that such negative wakes also exist in flows of various aqueous, shear-thinning, viscoelastic fluids around ellipsoids, ovoids, and cylinders. In this latter study, the flow around each object was examined for four types of fluids: a Newtonian fluid; an inelastic, shear-thinning fluid (3.5% carboxymethylcellulose, CMC, in water); a highly elastic, constant viscosity fluid (PAA in glucose); and several viscoelastic, shear-thinning solutions (1.5% and 2.5% PEO in water). In all of the non-Newtonian fluids, the fore-aft symmetry of the flow around the objects is broken with the most concentrated solutions displaying the most asymmetry. However, negative wakes were observed only for objects settling in fluids exhibiting both elastic and shear-thinning viscometric material properties. Additionally, the formation of the negative wake was dependent on exceeding a critical value of the elasticity number, defined as $E = De/Re$. This critical value was found to be lowest for blunt obstacles causing the greatest distortion of the fluid streamlines, i.e., cylinders and spheres.

Quantitative measurements of the negative wake were made by Bisgaard (1983), who used laser-Doppler velocimetry (LDV) to examine the kinematics around spheres and bubbles in a viscoelastic, shear-thinning solution of 1% PAA in glycerol. Negative wakes were present in all of the experiments, which covered a wide range of sphere-to-tube ratios $0.04 \le a/R \le 0.18$, Deborah numbers $11.4 \le De_0 \le 66.5$, and Reynolds numbers (based on the solvent viscosity) $0.0167 \le Re_s \le 0.29$. Additionally, Bisgaard observed temporal oscillations in the wake between the sphere and the point of flow reversal for $De_0 > 30.6$ that were manifested as rapid fluctuations in the axial velocity component only. At the largest Deborah numbers, these oscillations were dampened by the increased inertial effects resulting from shear-thinning in the fluid viscosity.

The previous studies have all arrived at the same qualitative description of the negative wake phenomenon; however, they have all used different fluids and different sphere-to-tube ratios making intercomparisons difficult. To address this deficiency, Bush (1994) performed a comprehensive series of experiments using the same fluid, a shear-thinning viscoelastic solution of 0.25% PAA in a corn syrup/water mixture, and the same apparatus. In these experiments, which differ from the previously discussed experiments in that the sphere is held fixed while the cylinder is translated at constant speed, Bush was able to proceed from a monotonically decreasing wake to the formation of a negative wake for the same sphere and cylinder by changing only the concentration of corn syrup in water from 80% to 30%. Bush attributed this behavior to the interplay between the elasticity of the fluid (quantified by the recoverable shear in viscometric flow) and the magnitude of the elongational stresses in the downstream region. Numerical calculations indicated that when there is little increase in the elongational viscosity and the elastic behavior appears to dominate, there is an upstream shift in the streamlines relative to the Newtonian case, which can lead to a negative wake. However, when the elongational stresses dominate, there is a monotonic downstream shift in the streamlines.

While the existence of a negative wake has been repeatedly documented experimentally, only recently have numerical models been able to predict such behavior. Numerical calculations by Jin et al. (1991), Zheng et al. (1991), and Bush (1994) appear to validate the experimental observation that both shear-thinning and elasticity, particularly an extensional-thickening viscosity, are necessary for the formation of a negative wake. In these calculations, four models – Newtonian, Carreau (shear-thinning, generalized Newtonian fluid), upper-convected Maxwell (constant-viscosity, elastic fluid), and Phan-Thien–Tanner (shear-thinning, viscoelastic fluid) – were used to calculate the velocity field around the sphere. Only when both shear-thinning and elastic effects were present, i.e., in simulations using the PTT model, was a negative wake predicted.

However, calculations by Satrape and Crochet (1994) using the FENE-CR dumbbell model have shown that a negative wake can be predicted using a constant viscosity, elastic fluid model. The computations show that the formation of a negative wake is intimately connected to the extensional properties of the constitutive model, particularly the FENE dumbbell extensibility parameter L. For small values of this parameter, $L^2 \sim 10$, a negative wake could be simulated for $De_0 > 1$. In more recent work by Harlen (1997), the differences between the kinematics of an Oldroyd-B fluid and a FENE-CR fluid with a small L value are examined more closely. Harlen argues that the velocity perturbation in the wake of the sphere depends on the relative magnitude of the elongational tensile stresses and the shearing stresses in the wake. For high Deborah number flows in which the polymer molecules are near full extension, the extensional stresses dominate, and when L is large the negative wake is not seen. However, when $L \sim O(1)$, the magnitudes of the tensile stresses are dramatically reduced and become of comparable magnitude to the shear stresses. Consideration of the gradients of each contribution to the stress then suggests that the rapid radial variations in the shear stress dominate the slow axial decay of the small tensile stresses and result in a negative wake.

Harlen et al. (1995) have also shown numerically that a negative wake develops at early times in the transient evolution of a wake in an Oldroyd-B fluid. As the sphere approaches steady state, this temporary negative wake disappears as the molecules in the wake become more highly oriented and elongated, and the large extensional stresses dominate the flow in the wake. Little is known experimentally about how the growth of this negative wake in the region behind a sphere accelerating from rest affects the initial transient motion of a freely sedimenting sphere or the final settling velocity of the sphere.

Regardless of the specific choice of model, or whether a shear-thinning viscosity is important, both Bush (1994) and Harlen (1997) point out that knowledge of the extensional rheology of the fluid is essential in understanding the evolution of the wake structure. As in other complex flow geometries, such as flow through an abrupt contraction (White and Baird, 1996), the numerical magnitude of a Deborah (or Weissenberg) number based on viscometric properties of the fluid is insufficient to discriminate between the response of different polymeric fluids or constitutive models. With the recent advent of filament stretching rheometers (Tirtaatmadja and Shidhar, 1993; Spiegelberg et al., 1996), it has become possible to accurately measure the transient extensional stress growth in mobile fluids such as polymer solutions. Measurements with an ideal PIB/PB

Boger fluid (with $L \sim 100$) indicate that these dilute polymer solutions show pronounced strain-hardening at moderate Hencky strains typical of those that can be experienced by fluid elements passing close by a sphere and into the downstream wake region. Direct LDV measurements and finite element calculations in the identical 0.31% PIB/PB fluid by Arigo et al. (1995) show that no negative wake forms and an elongated downstream wake structure develops.

The initial development of filament stretching devices was predicated on the assumption that the extreme strain-hardening and resulting large tensile stresses of ideal elastic Boger fluids would dominate the kinematics in the elongating filament. However, recent finite element calculations coupled with direct comparisons to experiments have shown that it is also possible to extract quantitative information about the transient extensional stress growth of concentrated polymer solutions (Kolte et al., 1997; Yao et al., 1998). Such materials show less strain-hardening, and they are characterized by shear-thinning viscometric properties that are best described by nonlinear constitutive equations, such as the K-BKZ or Giesekus models, incorporating multiple modes with a spectrum of relaxation times. Quantitative measurements of the transient extensional stress growth in polymer solutions thus appear possible, and filament stretching tests can be used to investigate whether the constitutive mechanisms for the formation of a negative wake discussed above are consistent with experimental observations.

In this paper, we experimentally investigate the structure of the negative wake in a shear-thinning, viscoelastic solution of 2% PAA in a 50/50 mixture of water/glycerin. In addition to characterization of the linear viscoelastic spectrum and the shear-thinning viscometric properties of the fluid, we use a filament stretching rheometer to measure the transient uniaxial extensional viscosity of the viscoelastic liquid. Using laser-Doppler velocimetry (LDV) and digital particle image velocimetry (DPIV), we examine the competing effects of elasticity, walls, and inertia on the negative wake. Additionally, full-field, two-dimensional DPIV results follow the transient formation of the negative wake as the sphere accelerates from rest.

Experimental setup

Falling sphere apparatus

The experimental test apparatus shown in Fig. 1 has been used in many studies on the motion of spheres by the authors (Becker et al., 1994; Arigo and McKinley, 1994; Arigo et al., 1995; Rajagopalan et al., 1996; Arigo and McKinley, 1997). The system consists of long plexiglass cylindrical tubes (1 m) of various internal radii, R, placed in a rectangular viewing box filled with a refractive index-matched fluid. Spheres of different radii, a, and density, ρ_s, are released via a mechanism that accurately aligns the sphere along the centerline of the tube. It has been well documented that spheres sedimenting off-axis will migrate towards the cylinder walls and rotate anomalously due to strong radial "lift" forces (Walters and Tanner, 1992; Becker et al., 1996). The digital video system used previously by the authors for investigating the transient motion of the sphere allows us to accurately monitor the deviations of the sphere from the centerline axis. The steady state settling velocity of the sphere, U_s, is measured via a timing method, i.e., the time of flight of the sphere is measured as it falls through a section of the tube far downstream of its release point using LED photo-diode detectors. The terminal velocity of spheres settling in polyacrylamide solutions depends greatly on the time interval between the release of successive spheres as a result of both the long relaxation timescale and the gel-like equilibrium structure of the fluid (Bisgaard, 1983; Walters and Tanner, 1992; Agarwal et al., 1994). Although this phenomenon is not investigated here, our measurements show excellent reproducibility when spheres are dropped at separation intervals greater than 15 min (Arigo and McKinley, 1997).

The flow field in the wake of the sphere is investigated using a single-color, fiber optic laser-Doppler velocimetry (LDV) system (Dantec Electronics, Inc.) coupled with a 300 mW argon-ion laser (Ion Laser Technology). The fluid is seeded with a small quantity of 0.22 μm titanium dioxide particles (TSI, Inc.), and the LDV system is carefully aligned with the centerline of the tube so that only the axial component of the fluid velocity around the sphere is measured. Utilizing a fast Fourier transform technique, the spectrum analyzer (Dantec Burst Spectrum Analyzer) computes the local fluid velocity from the Doppler-shifted frequency with an accuracy of ±0.5 mm/s. The use of a Bragg cell to impose a known frequency shift on one of the LDV laser beams allows negative velocities to be detected unambiguously. The mapping of the steady state velocity field from the unsteady Lagrangian laboratory reference frame of the LDV system to the steady Eulerian reference frame centered on the steadily translating sphere is performed by a simple Gallilean transformation $z = -(t - t_0) U_s$, where t_0 is the time at which the center of the sphere passes through the LDV measuring volume.

Such a transformation is not possible during the initial Eulerian-unsteady acceleration of the sphere. We therefore also measure the two-dimensional velocity fields utilizing a digital particle imaging (DPIV) technique. The same laser is coupled with a fiber optic light

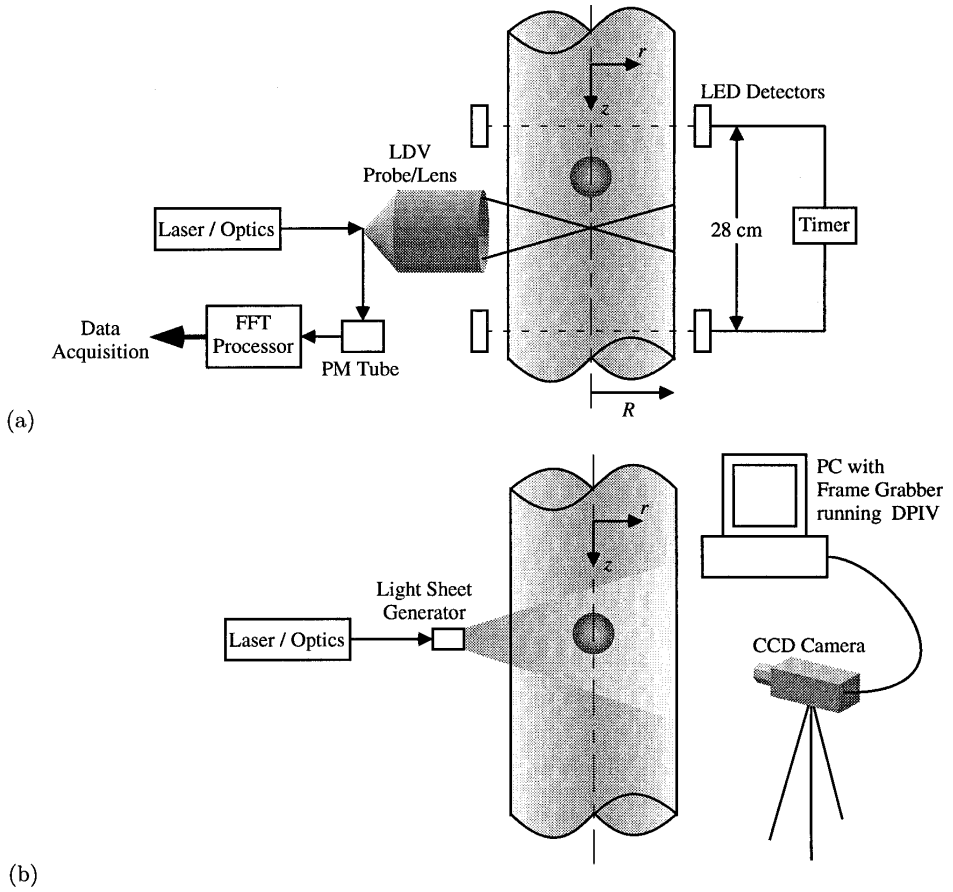

Fig. 1 Schematic diagram of the experimental apparatus including the laser-Doppler velocimetry system used to measure the centerline velocity around the sphere and the digital particle image velocimetry system used to obtain full-field velocity profiles of the flow around the sphere

sheet generator (Oz Optics), to illuminate an axial cross-section of the tube – approximately 7 cm in length (depending on camera magnification) and less than 1 mm thick. For this application, the fluid is seeded with a small volume fraction of 50 μm silver-coated glass spheres (Potters Industries), which provide good reflection in the laser light sheet. Using a high resolution gray-scale CCD camera, the motion of the seed particles as they follow the flow field is captured and digitized on a computer at rates up to 30 frames per second. Image pairs are then selected and analyzed by the DPIV algorithm, a correlating technique that calculates the average 2D particle displacement, Δx, in small corresponding sub-regions of the two images separated by a known timestep Δt. The DPIV implementation used here calculates the cross-correlations via fast Fourier transforms as implemented by Pakdel and McKinley (1997). These authors have analyzed the accuracy of this technique in a cavity flow geometry. An important assumption in all DPIV applications is that the flow remains two-dimensional so that particles remain within the viewing window.

Fluid rheology

The test fluid used in these experiments is a shear-thinning viscoelastic solution composed of 2.0 wt.% PAA in a 50/50 mixture of water and glycerol (fluid density, $\rho_f = 1.14$ g/cm^3). Arigo and McKinley (1997) have thoroughly characterized this solution in steady, transient, and oscillatory rheometric flows. Fig. 2 shows the steady and dynamic viscometric properties of this fluid. The zero-shear rate viscosity and first normal stress coefficient for the fluid are $\eta_0 = 464$ Pa·s and $\Psi_{10} \approx 1.15\times10^5$ Pa·s^2, respectively. Clearly, it is difficult to accurately determine $\Psi_{10} \equiv \lim_{\omega\to 0} 2\eta''/\omega$ from the data shown in Fig. 2 since the linear viscoelastic data at lower frequencies is subject to large fluctuations as the phase angle $\delta \to \pi/2$. However, the relaxation spectrum and the value $\Psi_{10} \approx 1.15\times10^5$ Pa·s^2 obtained from nonlinear regression to the dynamic linear viscoelastic data yields a parameter set that is consistent with other rheological tests including creep and startup of steady shear flow (Arigo and McKinley, 1997). A characteristic relaxation time for this fluid is $\lambda \sim \Psi_{10}/2\eta_0 \simeq 121$ s.

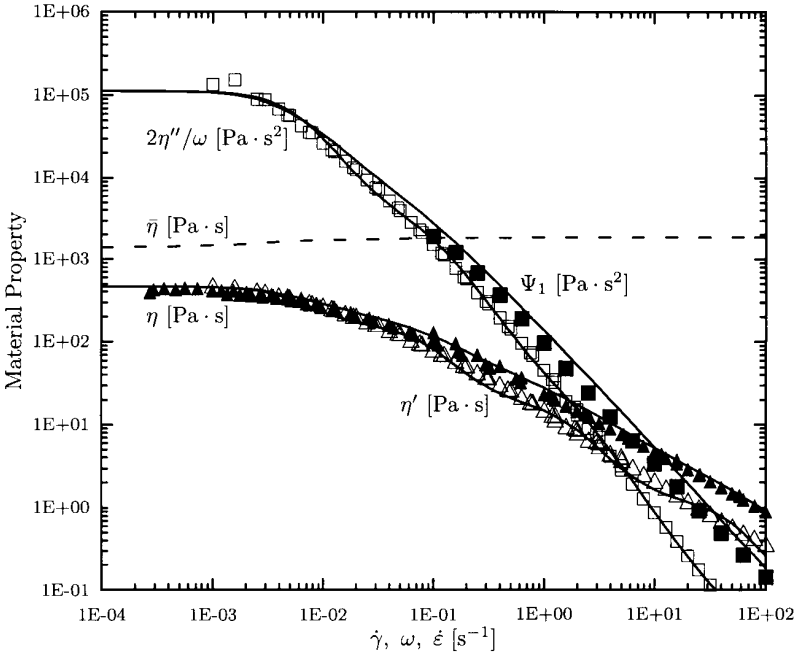

Fig. 2 Rheological properties of the shear-thinning, viscoelastic test fluid in steady shear flow (▲, ■) and small amplitude oscillatory shear flow (△, □). The solid lines are the predictions of the multimode Giesekus constitutive model for $\eta(\dot{\gamma})$, $\Psi_1(\dot{\gamma})$, and the dashed line is the predicted value of the steady uniaxial extensional viscosity $\bar{\eta}(\dot{\varepsilon})$ using the parameters specified in Table 1

Table 1 Multimode spectrum of viscosities, relaxation times, and nonlinear constitutive parameters for various models: linear viscoelasticity (LVE), Giesekus, and Phan-Thien-Tanner (PTT). The LVE spectrum is determined from nonlinear regression to dynamic, small amplitude oscillatory shear data $\{\eta', \eta''\}$ over the range of frequencies $0.001 \leq \omega \leq 100$ rad/s. The nonlinear parameters are fitted to the viscometric properties $\eta(\dot{\gamma})$ and $\Psi_1(\dot{\gamma})$ and the transient uniaxial extensional viscosity $\bar{\eta}^+(\dot{\varepsilon}, t)$

Mode, j	Linear viscoelasticity		Giesekus	Phan-Thien-Tanner	
	η_j [Pa·s]	λ_j [s]	a_j	ξ_j	ε_j
1	311.2	175.4	0.5	0.1	0.15
2	135.1	10.80	0.5	0.1	0.15
3	16.55	0.581	0.5	0.1	0.15
4	1.203	0.019	0.5	0.1	0.15
Solvent	0.006	–	–	–	–

This long timescale for build up of elastic stresses is important when characterizing transient flows of this fluid (Arigo and McKinley, 1997).

Table 1 lists the four-mode spectrum of relaxation times and viscosities determined from nonlinear regression to the dynamic, small amplitude oscillatory shear data. Arigo and McKinley (1997) have shown that the four-mode spectrum not only provides an excellent description of the rheological data, but can also be used to quantitatively describe the transient creep data in unsteady shearing flows as well as the initial acceleration of a sphere from rest. However, at steady state, we expect that because of the large fluid strains that develop, constitutive nonlinearities will dominate the fluid rheology. Thus, in addition to the linear viscoelastic spectrum (η_j, λ_j), we also include in Table 1 a fit of the Giesekus constitutive model parameter a_j and Phan-Thien–Tanner equation parameters ξ_j and ε_j. The choices of the parameter values are constrained by fitting to both the steady viscometric properties, $\eta(\dot{\gamma})$ and $\Psi_1(\dot{\gamma})$, and to measurements of the transient extensional viscosity, $\bar{\eta}^+(\dot{\varepsilon}, t)$, discussed further below.

The transient uniaxial stress growth in the fluid is measured using the filament stretching device developed by Spiegelberg et al. (1996). Small cylindrical fluid samples of initial radius $R_0 = 3.5$ mm and length $L_0 = 2.5$ mm are confined between rigid disks and elongated exponentially. In experiments with extremely strain-hardening materials and in numerical simulations with Oldroyd-B or FENE-type constitutive models, the imposed deformation approaches the ideal uniaxial elongation of a cylinder at long times. However, in more weakly strain-hardening fluids, the elongating filament retains the radially concave profile characteristic of a liquid bridge and the deformation is nonhomogeneous. Despite this non-ideality, recent simulations using a K-BKZ model and direct comparisons between finite element calculations with a multimode Giesekus model and filament stretching tests using a concentrated 5.0 wt.% polystyrene in dioctylphthalate (PS/DOP) solution have shown that it is still possible to extract *quantitative* information on the transient extensional stress growth in such materials (Kolte et al., 1997; Yao et al., 1998).

In the present tests, with a constant imposed strain rate $\dot{E}$, the upper plate is moved in accordance to a

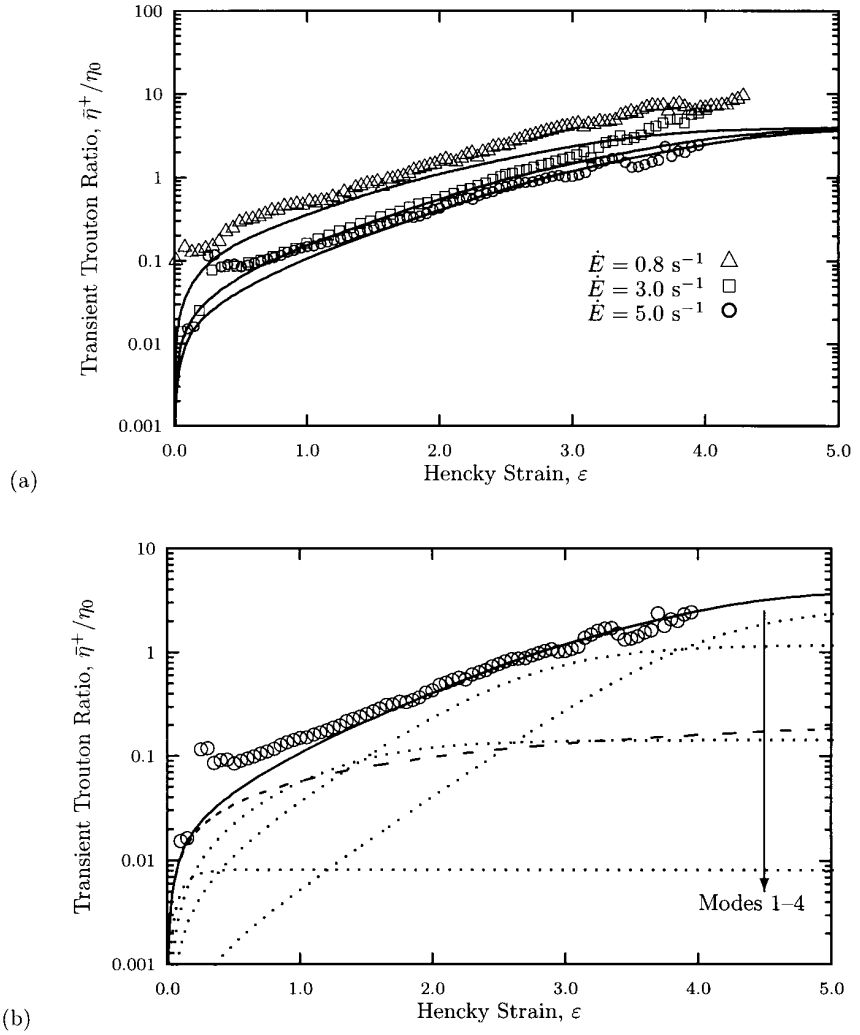

Fig. 3 Transient extensional viscosity $\bar{\eta}^+/\eta_0$ as a function of the Hencky strain. (a) Experimental results for extension rates of $\dot{E}=0.8$, 3.0, 5.0 s^{-1}. The solid lines are the predictions of the Giesekus model using the parameters imposed in Table 1. (b) The data at $\dot{E}=5.0$ s^{-1} from (a) showing the individual modal contributions of the Giesekus model for this strain rate (dotted lines) and the prediction of the multimode, generalized Maxwell model (dashed line)

single exponentially increasing velocity profile $V_p(t)=\dot{E}L_0\exp(+\dot{E}t)$, and the narrowest radius of the elongating filament $R_{min}(t)$ and the total tensile force $F_z(t)$ exerted on the stationary lower plate are measured. Following the notation of Kolte et al., this is a 'Type II' test and computational studies show that the extensional viscosity growth function in an ideal uniaxial deformation can be expressed as a transient Trouton ratio

$$Tr=\frac{\bar{\eta}^+(\varepsilon,De)}{\eta_0}=\frac{F_{z,corr}(t)}{\eta_0\,\dot{\varepsilon}_{eff}\pi R_{min}^2(t)} \qquad (1)$$

where the Deborah number is defined as $De=\lambda_1\dot{\varepsilon}_{eff}$. The force $F_{z,corr}$ is corrected to remove the contributions due to the gravitational body force and surface tension (both typically very small). The effective deformation rate, $\dot{\varepsilon}_{eff}$, experienced by the material element at the narrowest point in the filament is

$$\dot{\varepsilon}_{eff}=-\frac{2}{R_{min}(t)}\,\frac{dR_{min}}{dt}\,. \qquad (2)$$

At short times and small aspect ratios, experiments and calculations by Spiegelberg et al. (1996) show that the effective strain rate is $\dot{\varepsilon}_{eff}\approx 1.5\dot{E}$ in agreement with lubrication theory. At longer times, this value either increases or decreases slowly depending on the level of strain-hardening in the material. The total Hencky strain accumulated by a fluid element is found by integrating Eq. (2) to yield

$$\varepsilon(t)=\int_0^t\dot{\varepsilon}_{eff}(t')\,dt'=2\,ln\left(\frac{R_0}{R_{min}(t)}\right). \qquad (3)$$

The transient extensional stress growth in the shear-thinning 2 wt.% PAA/glycerin/water solution is shown in Fig. 3a. In contrast to experiments with dilute viscoelastic solutions such as Boger fluids, it is clear that there is no measurable Newtonian plateau ($\approx 3\eta_s/\eta_0$) at short times and that there is no dramatic increase in *Tr* at large strains. Experiments are performed at three dif-

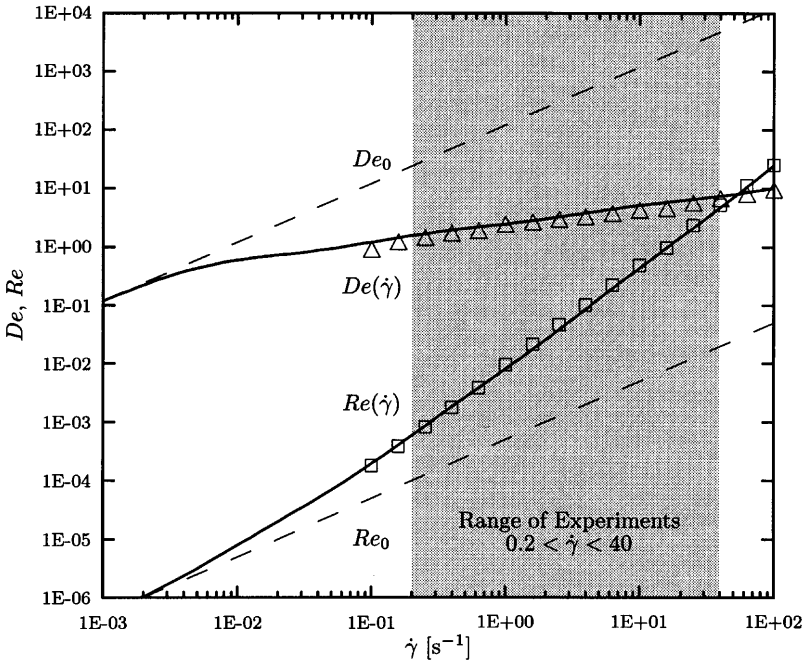

Fig. 4 The range of shear-rate-dependent and zero-shear-rate Deborah numbers ($De(\dot{\gamma})$, De_0) and Reynolds numbers ($Re(\dot{\gamma})$, Re_0) encompassed in this paper. The symbols represent the experimental values computed from steady rheological measurements of $\Psi_1(\dot{\gamma})$ and $\eta(\dot{\gamma})$, while the solid lines are from the Giesekus fit to the steady shear rheology. Dashed lines are zero-shear-rate properties based on $\eta_0 = 464$ Pa·s and $\lambda = 121$ s. Reynolds numbers are calculated using a sphere radius of $a = 1.27$ cm

ferent nominal extension rates $\dot{E} = 0.8$, 3.0, and 5.0 s^{-1} characteristic of the deformation rates (U_s/a) attained in the settling sphere tests described below. At large strains, similar levels of tensile stress growth are observed in each test; however, at short times, the value of *Tr* decreases with increasing strain rate when plotted as a function of the Hencky strain. This is characteristic of the initial linear-viscoelastic-like response of a material in which the stress is best represented as a function of t/λ_1. Given the large spectrum of relaxation times in the test fluid (see Table 1) and the limited Hencky strains that can be achieved, this region is expected to last throughout the whole test.

The solid curves shown in Fig. 3a are the predictions of the four-mode Giesekus model in a homogeneous ideal uniaxial elongational flow computed using a fourth order Runge-Kutta integration routine. In these simulations, the Deborah number for each mode is $De_j = \lambda_j \dot{E}$. The deviation between the model prediction at short times ($\varepsilon < 0.5$) arises from the initial shear flow in the filament stretching device. At moderate strains ($0.5 \leq \varepsilon \leq 3$), the magnitude of the stress growth and the trend with increasing $\dot{E}$ is accurately captured by the multimode model. At larger Hencky strains ($\varepsilon > 3$), the data systematically deviates from the numerical predictions, and the fluid appears to be slightly more strain hardening than predicted by the constitutive model. The experiments at large strains are extremely difficult to perform since the tensile force in the filament rapidly decays towards zero and the effective strain rate, $\dot{\varepsilon}_{eff}$, increases with time as the filament necks down in the midregion and fails or ruptures in a finite time at a critical strain, $\varepsilon \sim 4.5$ as shown by Yao et al. (1998). The most important factor to note is that in contrast to measurements at identical strains and strain-rates in semi-dilute PIB Boger fluids, the transient Trouton ratio is $Tr \sim O(10)$, not $Tr \sim O(1000)$ (Tirtaatmadja and Shidhar, 1993; Spiegelberg et al., 1996).

In Fig. 3b we show in greater detail the prediction of the multimode Giesekus model for the stretch rate of $\dot{E} = 5.0$ s^{-1}. The solid line corresponds to the total tensile stress given by summing each individual mode (shown by dotted lines). The linear viscoelastic response predicted by the generalized linear Maxwell model with *n* modes is given by

$$\frac{\bar{\eta}^+(\dot{\varepsilon}_{eff}, t)}{\eta_0} = 3 \sum_{j=1}^{n} \eta_j \left(1 - e^{-t/\lambda_j}\right) \qquad (4)$$

and is shown by the broken line. It is clear that at these stretch rates the fluid behaves in a weakly nonlinear manner with only moderate strain-hardening. For simplicity in modeling this response, we have chosen to use the multimode Giesekus model with a single value of the network mobility parameter a for all modes. We acknowledge that a better fitting to the rheology can be achieved by fitting a different a_j for each mode. However, it is clear from Figs. 2 and 3 that a good fit to both the steady shear and the transient extensional data can be attained with $a_j = 0.5$ for all modes. Decreasing a_j increases the level of strain-hardening in Fig. 3a but also lowers the extent of shear-thinning and over-predicts the data in Fig. 2. An alternate approach is to select a nonlinear model with separate parameters to con-

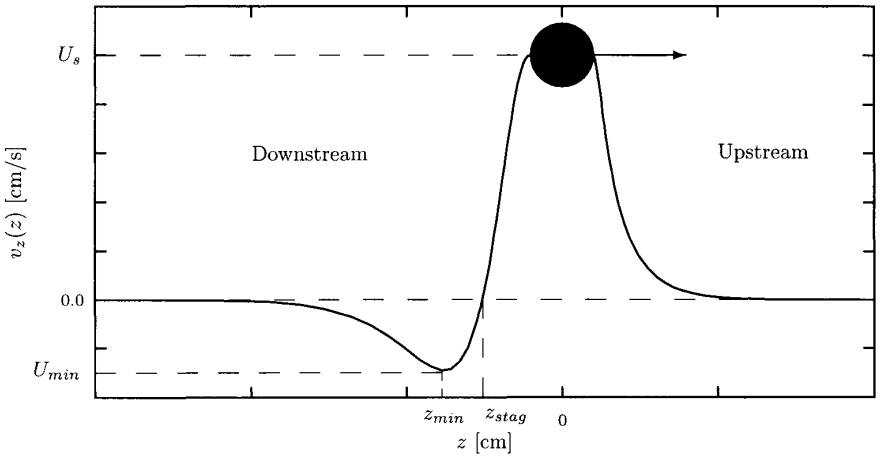

Fig. 5 A sketch of a typical negative wake indicating the key features of the velocity profile in a laboratory reference frame with the origin located at the center of the sphere at time t_0. The maximum negative velocity is denoted U_{min} and is located at z_{min}. The stagnation point where the flow reverses in the wake of the sphere is located at z_{stag}

trol the shear-thinning and strain-hardening, such as the Phan-Thien–Tanner model, which is discussed in the Appendix.

In order to accurately quantify the relative importance of elastic, viscous, and inertial effects in the complex flow past a sphere, we report shear-rate–dependent values of the Deborah number (often referred to as the recoverable shear)

$$De(\dot{\gamma}) = \lambda(\dot{\gamma})\,\dot{\gamma} = \left\{ \frac{\Psi_1(\dot{\gamma})}{2\,[\eta(\dot{\gamma}) - \eta_s]} \right\} \tag{5}$$

and the Reynolds number

$$Re(\dot{\gamma}) = \frac{\rho_f\, a^2\, U_s}{\eta(\dot{\gamma})} \tag{6}$$

where the characteristic deformation rate is based on the experimentally measured steady state velocity U_s of the sphere $\dot{\gamma}=U_s/a$. The reported values of $De(\dot{\gamma})$ and $Re(\dot{\gamma})$ are calculated using the multimode Giesekus parameters.

The incorporation of shear-thinning effects is necessary because of the extreme shear-thinning observed in the material functions for this fluid, e.g., for a 1.27 cm diameter aluminum sphere ($\rho_s = 2.79$ g/cm^3) sedimenting at a velocity of $U_s = 1.03$ cm/s, the shear rate is $\dot{\gamma} = 0.811$ s^{-1}, corresponding to $De_0 = 98$, $De(\dot{\gamma}) = 2.32$, $Re_0 = 3\times10^{-4}$, and $Re(\dot{\gamma}) = 5\times10^{-3}$. A consequence of using shear-rate dependent Deborah numbers is that the range of De spanned experimentally is greatly contracted, given the density of spheres which were used in these experiments ($2.17 \le \rho_s \le 8.53$ g/cm^3). The variations in the functions $De(\dot{\gamma})$ and $Re(\dot{\gamma})$ with shear rate are shown in Fig. 4. In order to regain the linear viscoelastic limit, experiments at shear rates $\dot{\gamma} \le 10^{-3}$ are required. For a 1.27 cm radius sphere, this corresponds to a sedimentation velocity of 12.7 μm/s or a density contrast of $\alpha = \rho_s/\rho_f \approx 1.003$. Although we report our results in terms of $De(\dot{\gamma})$ and $Re(\dot{\gamma})$, the zero–shear-rate quantities can be obtained from Fig. 4 if desired.

Experimental results

We now turn to detailed measurements of the fluid kinematics, $\boldsymbol{v}(\boldsymbol{x})$, surrounding the sphere as it settles in the cylinder at a steady state velocity, U_s. Dimensional analysis suggests that this motion will depend on the density contrast between the sphere and the fluid, $\alpha = \rho_s/\rho_f$, the sphere-to-tube aspect ratio, a/R, and the Reynolds number, $Re(\dot{\gamma})$, characterizing inertial effects. Fig. 5 illustrates the important aspects of the flow field. The sphere translates from left to right in the direction of increasing z at a steady velocity U_s. The maximum negative velocity is denoted U_{min} and is located at z_{min}, and the stagnation point in the wake where the flow reverses is located at z_{stag}. Measurements of the viscoelastic corrections to the steady state drag force acting on the sphere have been reported in our previous publication (Arigo and McKinley, 1997) and are not included here. Any elastic modifications to the drag resulting from the evolution in the wake structure documented below are dominated by the shear-thinning properties of the fluid rheology, and a purely inelastic correlation is found to be sufficient to describe the drag correction factor.

Effect of density contrast

In Figs. 6 and 7, LDV measurements of the fluid velocity around the sphere along the centerline of the cylinder are presented. In these figures, we plot the axial component of the fluid velocity, v_z, versus the axial coordinate, z. Here, the cylindrical coordinate system z is centered on the sphere and oriented in the direction of

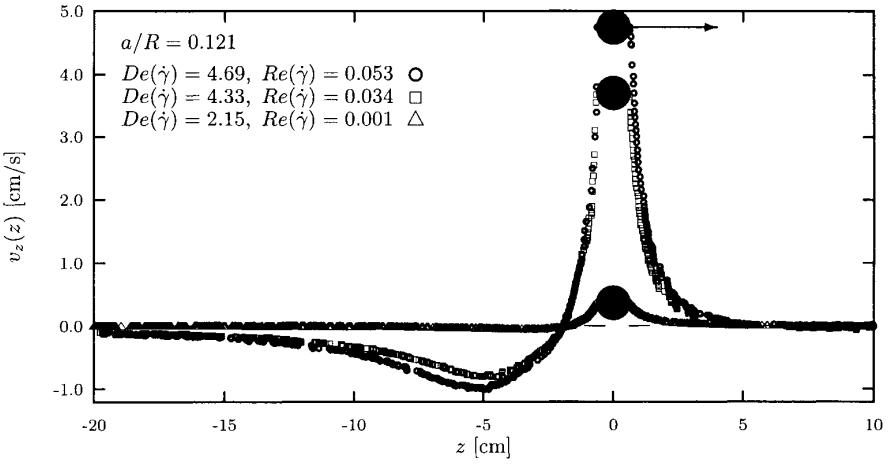

Fig. 6 Experimentally measured steady state velocity profiles for the flow of a shear-thinning, viscoelastic fluid along the centerline of a cyclinder in the vicinity of a sphere. The sphere-to-tube ratio is $a/R = 0.121$ and varying density contrasts, $\alpha = 3.37$, 6.82 and 7.48, are used to generate the increasing values of *De*

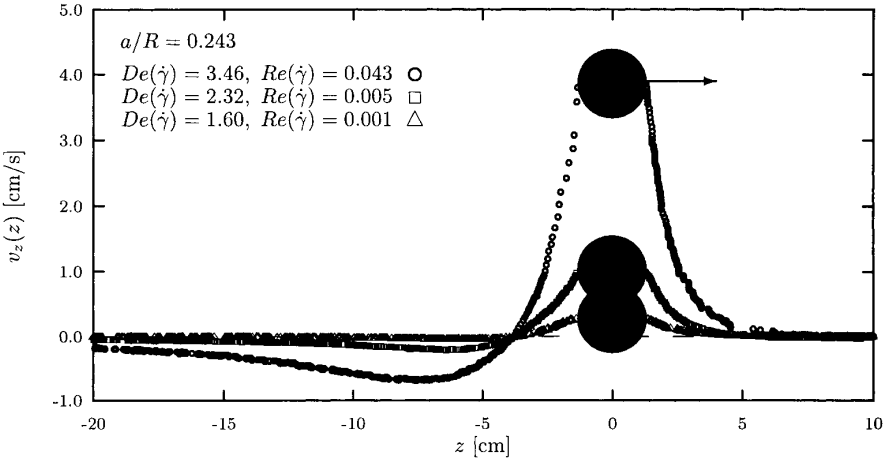

(a)

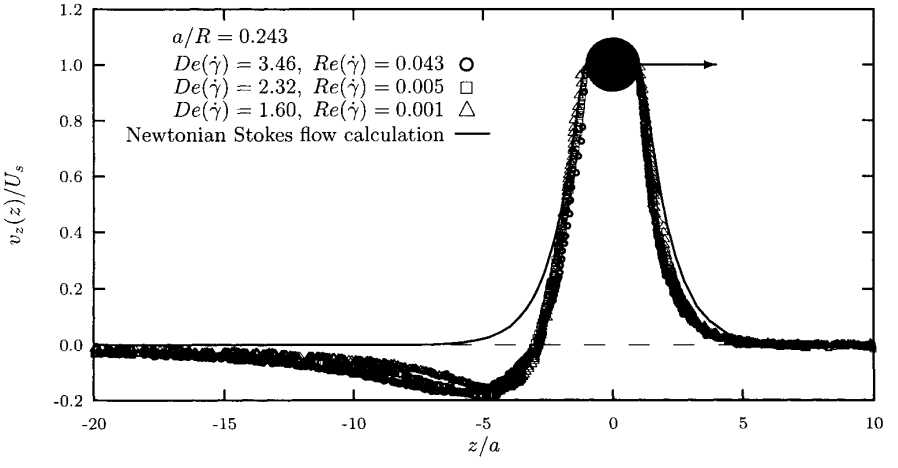

(b)

Fig. 7 Experimentally measured velocity profiles for the steady motion of a shear-thinning, viscoelastic fluid along the centerline of a cylinder for a sphere-to-tube ratio of $a/R = 0.243$ and varying density contrasts $\alpha = 1.90$, 2.45 and 3.38. The coordinate system is centered on and traveling with the sphere. (a) Dimensional scales and (b) dimensionless scales normalized with the steady state velocity U_s and the sphere radius *a*

travel so that positive values of *z* represent unperturbed fluid upstream of the sphere, while $z < 0$ is the wake region behind the sphere. Far upstream of the sphere, the fluid is quiescent ($v_z = 0$), and the velocity monotonically rises to the velocity of the sphere at the front stagnation point, $z = a$. The extent of the upstream velocity disturbance is confined within a distance $z \sim R$ or $z/a \sim R/a$ for all experiments shown here, in agreement with computations for a Newtonian fluid shown by the solid line in Fig. 7b. There is a slight deviation

from the Newtonian creeping flow upstream of the sphere and, at any given axial position, velocities in the viscoelastic fluid are below the Newtonian limit. This deviation was also noted by Sigli and Coutanceau (1977) and arises from the gradual decrease in the fluid viscosity as the deformation rate increases progressively closer to the sphere.

In the downstream wake of the sphere, the fluid velocity decays back to zero; however, for all of the measurements presented in the present work, this decay is not monotonic. In the region immediately behind the sphere, $z_{stag} \le z \le -a$, the fluid velocity decays very rapidly to zero. This decay is much faster than that seen in the wakes of either a Newtonian fluid or a constant viscosity Boger fluid. In the former case, the velocity decay in the wake is confined by $z/a \sim -R/a$ for creeping flow (see Fig. 7b). In the latter case of Boger fluids, the wake has been found to extend to distances beyond $z/a \sim -30$ downstream before returning to zero velocity (Bush, 1993; Arigo and McKinley, 1994; Arigo et al., 1995).

In both Fig. 6 ($a/R = 0.121$) and Fig. 7a ($a/R = 0.243$), which show the *dimensional* velocity profiles, the position of the stagnation point z_{stag} is located at the same downstream distance for all densities and Deborah numbers shown. For both aspect ratios, this point is $z_{stag}/a \sim -3.0$ as shown in Fig. 7b. The fixed location of the stagnation point suggests that the dynamics which control the formation of this stagnation point in this fluid are independent of the Deborah number and are primarily affected by the geometry, i.e., the sphere radius a and the cylinder radius R.

This scaling is supported by Fig. 7b in which the velocity is normalized with the steady state velocity, U_s, and axial distances are scaled with the sphere radius, a. In this plot, the fluid velocities in the downstream region $z_{stag} \le z \le -a$ superimpose to form a single curve, indicating that, again, this section of the flow is independent of the Deborah numbers spanned experimentally.

A similar scaling was not observed in the earlier work of either Sigli and Coutanceau (1977) or Bisgaard (1983). For an aspect ratio, $a/R = 0.25$, Sigli and Coutanceau found that the location of z_{stag} increases slightly with increasing Deborah numbers in the range $0.022 \le De_0 \le 0.120$. The range of values reported by Sigli and Coutanceau, $-3.1 \le z_{stag}/a \le -2.5$, for this aspect ratio is similar to the value found in the present work for aspect ratios $a/R < 0.396$. For larger aspect ratios, $a/R = 0.5$ and 0.75, Sigli and Coutanceau report a much stronger dependence of z_{stag} on aspect ratio. For these experiments, increasing the sphere-to-tube ratio shifts z_{stag} upstream closer to the sphere, $z_{stag} \sim 1.8$.

In Bisgaard's (1983) experiments which span the range $0.04 \le a/R \le 0.18$ and $11.4 \le De_0 \le 66.5$, the stagnation point was located much farther downstream, $z_{stag}/a < -17$. However, these experiments did show that z_{stag} was constant for $De_0 \le 30.6$, the only flows that Bisgaard reported as stable. Flows beyond this critical Deborah number were reported as unstable due to the onset of transient oscillations in the axial velocity within the region $z_{stag} \le z \le -a$, and the location of the stagnation point approaches $z_{stag}/a \sim -70$.

At downstream locations beyond the flow reversal point $z < z_{stag}$, the fluid velocity becomes negative, $v_z(z) < 0$, and continues to decrease monotonically until reaching a minimum velocity, U_{min}. The position of the minimum velocity, z_{min}, is a function of the Deborah number and is shifted farther downstream as $De(\dot{\gamma})$ increases. Additionally, the magnitude $|U_{min}|$ increases with increasing $De(\dot{\gamma})$, and, as shown in Fig. 7b, U_{min} scales with the steady state velocity of the sphere, a trend also noted by Bisgaard (1983). As in Bisgaard's experiments, the negative wake ratio, $NW \equiv |U_{min}/U_s|$, was found to be constant for all Deborah numbers and aspect ratios; however, in the present work, $NW \approx 0.15$ for all *low* Reynolds number experiments, while Bisgaard reports a much smaller value, $NW \approx 0.037$. The results of Sigli and Coutanceau (1977) show that NW increases with increasing De_0 and a/R within the range $0.06 \le NW \le 0.25$ for their experiments. These variations in the kinematic characteristics of the negative wake structures presumably arise from rheological differences in the three different concentrated polymer solutions; in particular, the levels of strain-hardening and shear-thinning developed in the complex flow near the sedimenting sphere.

Beyond the point z_{min}, the fluid velocity monotonically decays to zero over a long distance. In all cases, the extent of the negative wake extends more than 20 radii downstream with the heavier spheres falling at the highest Deborah numbers having the longest wakes. This axial expansion of the elastic wake structure is similar to that observed in Boger fluids and is due to the strong extensional flow in the wake of the sphere resulting in large extensional stresses that slowly relax on a timescale $t \sim \lambda_1$.

DPIV results of the fluid motion around the sphere are presented in Fig. 8. In Fig. 8a, a "streak" photograph image is shown, which is the superposition of the two consecutive images used to calculate the DPIV vector field shown in Fig. 8b. In this figure, a ceramic sphere ($\rho_s = 3.84$ g/cm^3, $a = 0.635$ cm) settles in the test fluid such that the steady state settling velocity is $U_s = 0.412$ cm/s or equivalently $De(\dot{\gamma}) = 2.19$ and $Re(\dot{\gamma}) = 0.001$. In this figure, we focus on three distinct regions of the flow field close to the sphere: the front, the side, and the rear.

In the front of the sphere, the velocity field is essentially Newtonian. Fluid is pushed out radially in front of the sphere and circulates around to the rear of the sphere. Note that the center of the recirculating region

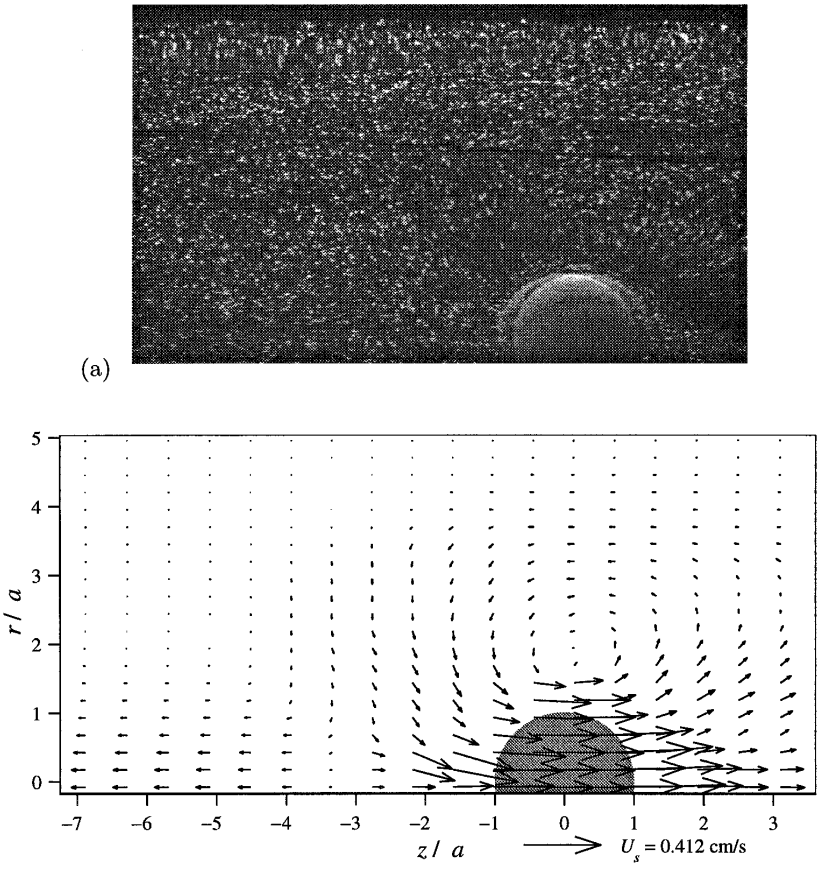

Fig. 8 Quantitative velocity field determined using DPIV for a 0.635 cm radius, ceramic sphere settling at $U_s = 0.412$ cm/s: $a/R = 0.196$, $\alpha = 3.37$, $De(\dot{\gamma}) = 2.19$, $Re(\dot{\gamma}) = 0.001$. (a) Streak photograph of the flow. (b) Vector field calculated using DPIV

along the side of the sphere is not centered between the sphere's equator and the cylinder wall, but is much closer to the sphere. This is a result of the heavy shear-thinning of the fluid in this narrow region where the local shear rates attain their maximum values. By contrast, in a Newtonian fluid at zero Reynolds number, the recirculation is locally centered within this region, while calculations of constant viscosity, elastic fluid models show that the recirculation is shifted slightly towards the cylinder wall (Jin et al., 1991; Arigo et al., 1995).

Downstream of the sphere, we observe the formation of the negative wake structure, and almost the entire wake is captured in this image. There is a strong flow in the opposite direction to the sphere, confined mainly within a region bounded by a radial distance $r \sim a$. This is due to the large radial gradients in shear stress that develop from the centerline towards the equator of the sphere that counteract the strong extensional flow in the wake behind the sphere (Harlen, 1997). To preserve continuity, this flow is balanced by a weak inward flow towards the centerline from regions near the cylinder wall. Note that the center of this secondary recirculating region is located at $r \sim R/2$. Similar DPIV images and results were obtained for other aspect ratios and Deborah numbers (see Fig. 10).

Effect of geometric aspect ratio

In Figs. 9a and 9b, we show LDV measurements comparing spheres of the same density ratio and different radii falling in a cylinder of radius $R = 5.23$ cm. In Fig. 9a, the kinematic effects of the varying aspect ratio are clearly shown in dimensional form. Upstream, the velocity disturbance is confined within a region bounded by the radius of the cylinder $z \sim R$, while downstream, increasing the aspect ratio magnifies the negative wake and shifts it further downstream. Although the spheres fall at different speeds, the characteristic shear rate, U_s/a, in each case is approximately the same. Hence, the final Deborah numbers for the spheres in this figure were nearly identical, and so, in some sense, we are examining only the effects of the proximity of the cylinder walls.

In Fig. 9b, these measurements are normalized using the steady sphere velocity, U_s, and the sphere radius, a. Again, upstream of the sphere there is a purely geometric effect that scales the upstream extent of the flow with $z/a \sim R/a$. However, downstream, the results superimpose almost completely. There is a slight deviation beyond z_{min} where decreasing the aspect ratio, a/R, shifts the location of U_{min} as well as the remainder of

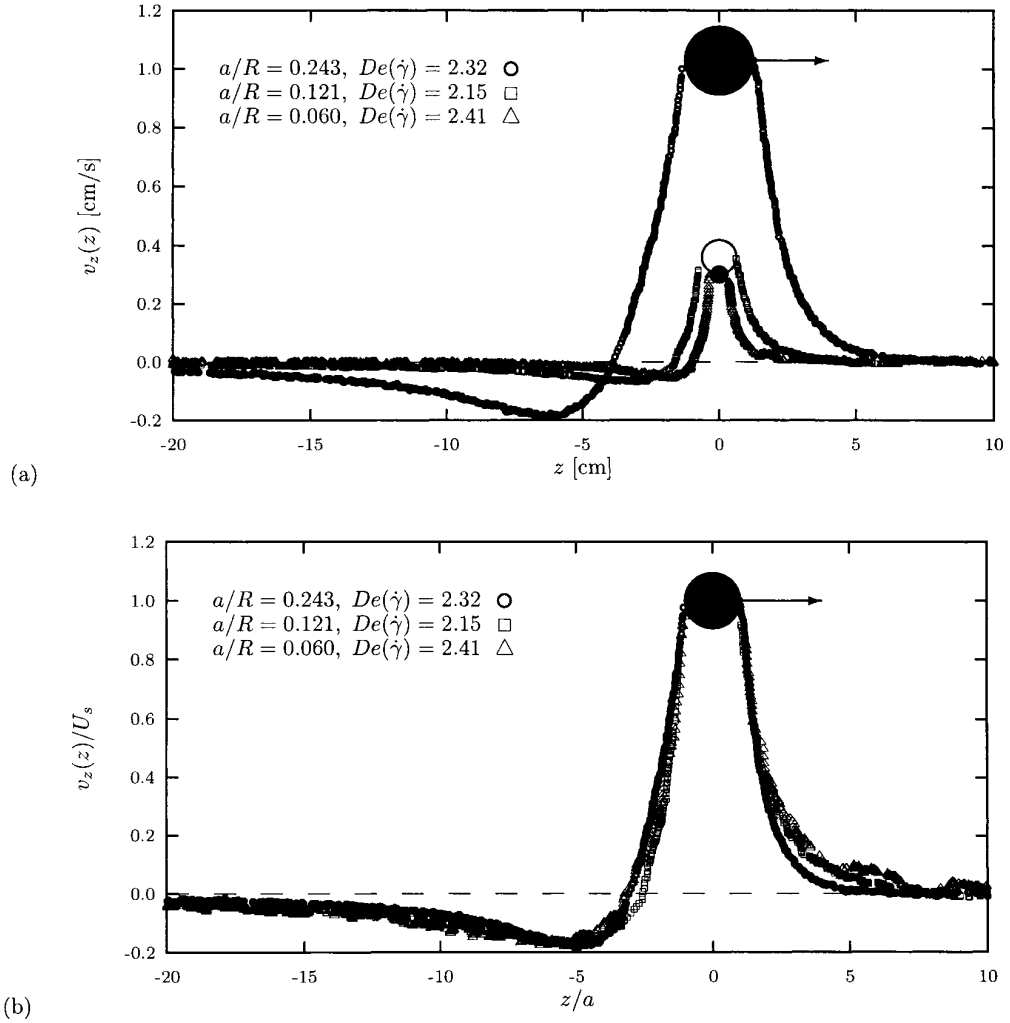

Fig. 9 Effects of changing aspect ratio a/R on the centerline fluid velocity profiles around a sphere. (a) Dimensional scales and (b) dimensionless scales normalized with the steady state velocity U_s and the sphere radius a

the decaying wake beyond z_{min} slightly downstream. Sigli and Coutanceau (1977) also examined the effect of a/R by pulling spheres through the fluid along the centerline of a cylinder at a fixed velocity. For moderate aspect ratios, $a/R = 0.25$, 0.5, and 0.75, at fixed low $De_0 = 0.04$, increasing the aspect ratio was found to shift both z_{stag} and z_{min} towards the sphere and magnify the magnitude of the negative wake, *NW*.

Fig. 10 shows a sequence of DPIV velocity fields around a 1.27 cm radius aluminum sphere settling in a cylinder of radius $R = 3.28$ cm. Qualitatively, the flow field in these images is identical to that seen in Fig. 8 for a smaller sphere in the same tube. Fluid is pushed out in front of the sphere (Fig. 10a), recirculates around the side (Fig. 10b), and is drawn in behind the sphere (Fig. 10c). Because of the smaller distance between the sphere and the cylinder wall and the higher shear rates in this region, the center of the recirculation around the side of the sphere is much closer to the sphere than in Fig. 8. Within the negative wake region, the strongest flow is again confined radially within a region $r \sim a$ where the extensional effects are strongest.

Finally, we note that in Fig. 9 a negative wake forms for even the smallest aspect ratio examined in this paper, $a/R = 0.060$. This result complements Bisgaard's (1983) work with small aspect ratio experiments, and it indicates that the negative wake is a phenomenon that would exist even in an unbounded domain, i.e., the mechanism responsible for the formation of a negative wake arises from the complex shear and extensional flow in the immediate wake of the sphere, not from the lateral confining effects of the cylinder walls.

Effect of inertia

Fig. 11 compares the structure of the negative wake for two spheres, one sedimenting at low Reynolds number, $Re(\dot{\gamma}) = 0.005$, and the other at high Reynolds number,

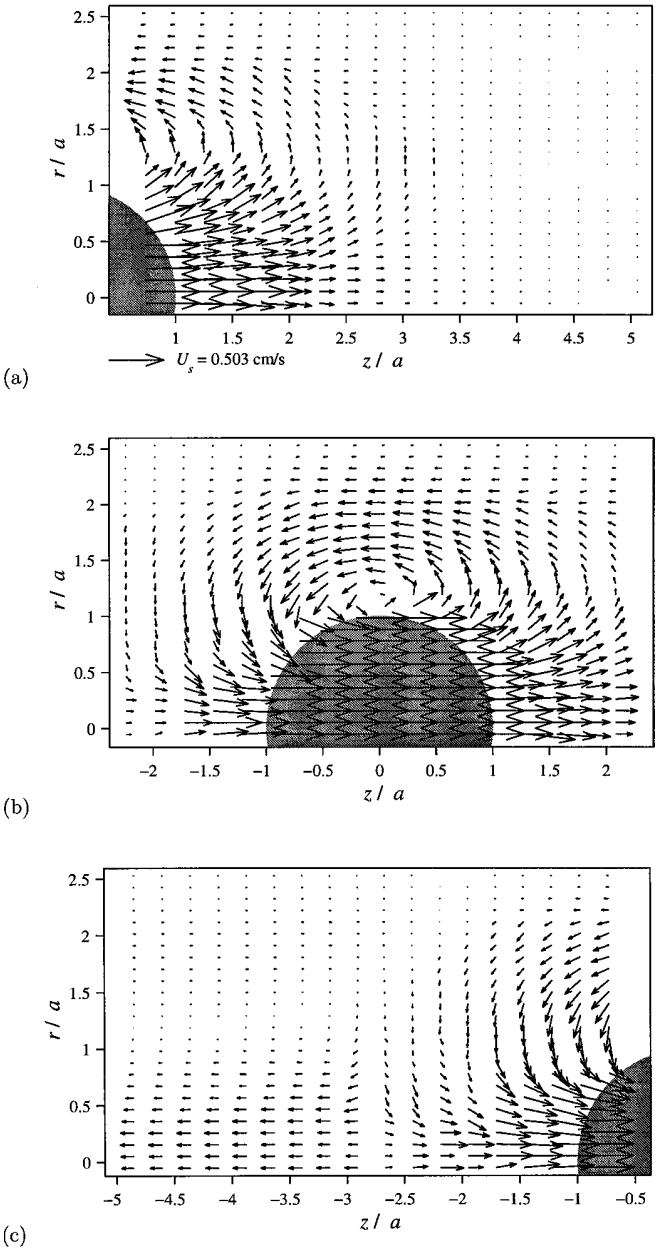

Fig. 10 DPIV velocity fields for a 1.27 cm radius, aluminum sphere settling at $U_s = 0.503$ cm/s: $a/R = 0.396$, $\alpha = 2.45$, $De(\dot{\gamma}) = 1.93$, $Re(\dot{\gamma}) = 0.001$. (a) In front of the sphere, (b) along the side of the sphere, and (c) behind the sphere

$Re(\dot{\gamma}) = 9.4$, together with the predicted velocity profile for creeping flow of a Newtonian fluid. Both spheres develop negative wakes; however, inertial effects highly distort the structure of the wake for the faster-moving sphere. The wake is shifted much farther downstream: $z_{stag}/a \approx -13$. Additionally, the magnitude of the negative wake, *NW*, also decreases from $NW \approx 0.15$ (characteristic for all the low Reynolds number experiments presented here) to $NW \approx 0.10$. These results are more compatible with the LDV experiments of Bisgaard (1983), who reported $z_{stag}/a < -17$ and $NW \approx 0.037$, even though the Reynolds numbers based on the solvent viscosity reported by Bisgaard are very small, $0.0167 \leq Re_s \leq 0.29$.

Transient evolution of the negative wake

Arigo and McKinley (1997) have previously discussed the transient motion of a sphere accelerating from rest in this fluid and geometry. Fig. 12, reproduced from that reference, shows the transient velocity of an aluminium sphere accelerating from rest along the centerline of a tube such that $\alpha = 3.38$ and $a/R = 0.243$. Here, we see the effects of the complex fluid rheology on the motion of the sphere. The sphere undergoes several oscillations about the final steady state velocity, including a "rebound" during the first oscillation in which the sphere stops and reverses direction momentarily before continuing to sediment down the axis of the cylinder. Although this initial transient response of the sphere is very well described by an analysis incorporating the linear viscoelasticity of the fluid and the inertia of the sphere, such a model does not predict the formation of a negative wake in the fluid kinematics or the decrease in the steady state drag on the sphere. Additionally, there are currently no numerical simulations that examine the progressive development of the negative wake structure as the strain in the fluid increases from rest. Numerical calculations by Harlen et al. (1995) show that, even in a constant viscosity elastic fluid, this transient evolution of the velocity field can be extremely complex.

Figs. 13a–h represent a series of DPIV images for a single experiment that follows the transient evolution of the negative wake as the sphere accelerates from rest. These images of the fluid velocity field are cross-referenced to Fig. 12, which details the transient velocity of the sphere, $U_s(t)/U_s$ and displacement of the sphere from rest, $z(t)/a$, at the appropriate times.

Figs. 13a–c show the acceleration of the sphere up to the initial velocity overshoot. On the scale of the finite time increment resolvable by the CCD camera (0.033 s), the fluid response appears instantaneous since the fluid is initially very viscous. Vorticity information from the accelerating sphere diffuses to the boundaries very rapidly ($t_{diff} = a^2/\nu \approx 0.003$ s), and a "Newtonian-like" velocity field is set up as fluid is displaced in front of the sphere, circulated around the side, and drawn in at the rear. At each stage in the first three figures, the flow can almost be considered quasi-steady as the velocity field changes primarily in magnitude only, although closer inspection shows that the center of the recirculating fluid motion slowly moves away from the

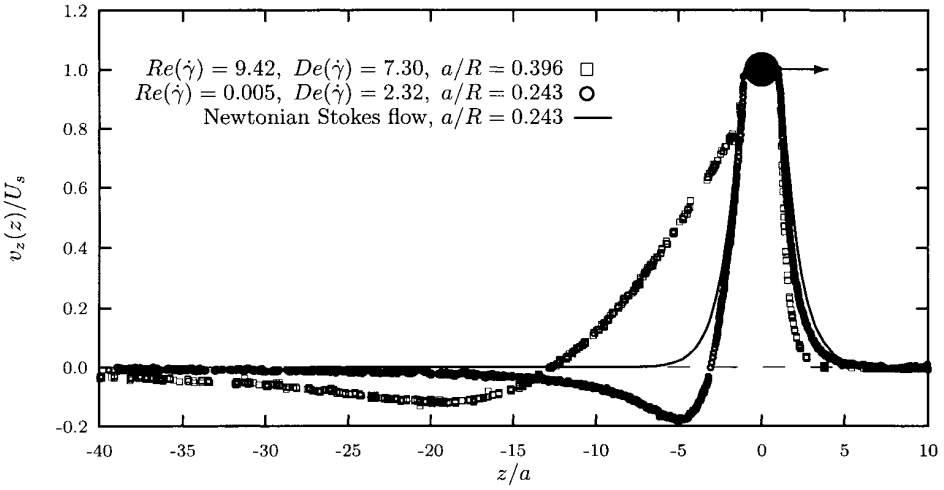

Fig. 11 Effects of inertia on the centerline fluid velocity profiles around a sphere. Results are normalized with the steady state velocity U_s and the sphere radius a

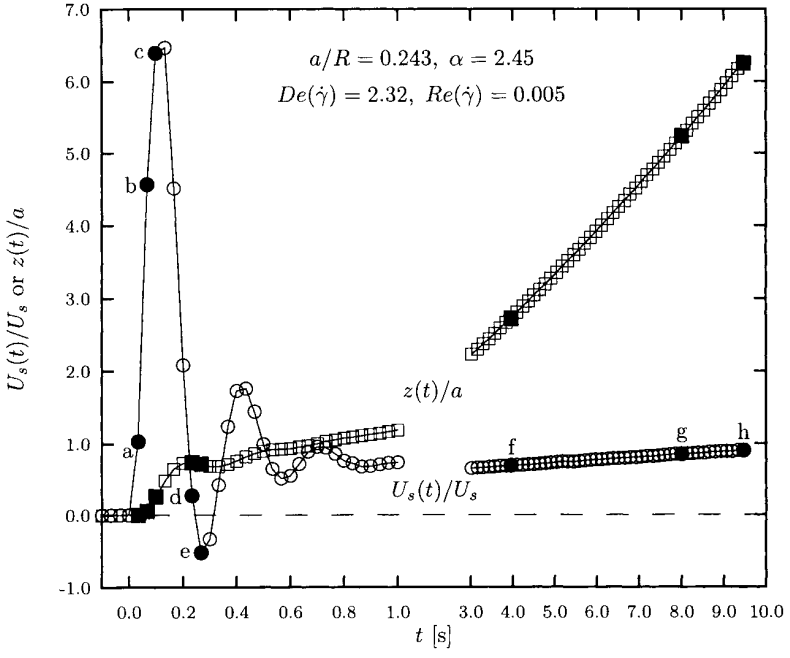

Fig. 12 The dimensionless initial transient velocity, $U_s(t)/U_s$ (○), and displacement from rest, $z(t)/a$ (□), of a 1.27 cm radius ceramic sphere accelerating from rest under the influence of gravity along the centerline of a cylinder. $a/R = 0.243$, $\alpha = 2.45$, $De(\dot{\gamma}) = 2.03$, $Re(\dot{\gamma}) = 0.006$. The solid data points indicate the temporal location of the DPIV vector fields shown in Fig. 13. Note the break in the abscissa from $t = 1.0$ to 3.0 s

sphere. The treatment of the motion of the sphere as quasi-steady has been discussed in detail by Arigo and McKinley (1997).

In the subsequent two figures, the sphere comes to rest momentarily (Fig. 13d) and then "rebounds" (Fig. 13e). As the sphere reverses its direction, so does the flow field, forming the same recirculating structure in the opposite direction. To this point, no negative wake is observed in these DPIV images.

The final three figures show the formation of the negative wake at longer times. Fig. 13f jumps ahead to $t = 3.967$ s when the sphere is again settling down the cylinder under the action of gravity. At time $t = 8.00$ s, the formation of a weak negative wake begins. At this point, the sphere has fallen a dimensionless distance (or experienced a global strain) of

$$\gamma = \int_0^t \frac{U_s(t)}{a}\, dt = \frac{z(t)}{a} \approx 5.0\,. \tag{7}$$

This clearly indicates that the negative wake is a large strain phenomenon associated with nonlinear viscoelasticity. For small characteristic strains, the polymer molecules are not sufficiently extended and the tensile stresses in the wake are not sufficiently developed for the negative wake to form. However, at Hencky strains of $\varepsilon = \ln(1+\gamma) \approx 1.8$, the polymer solution exhibits an al-

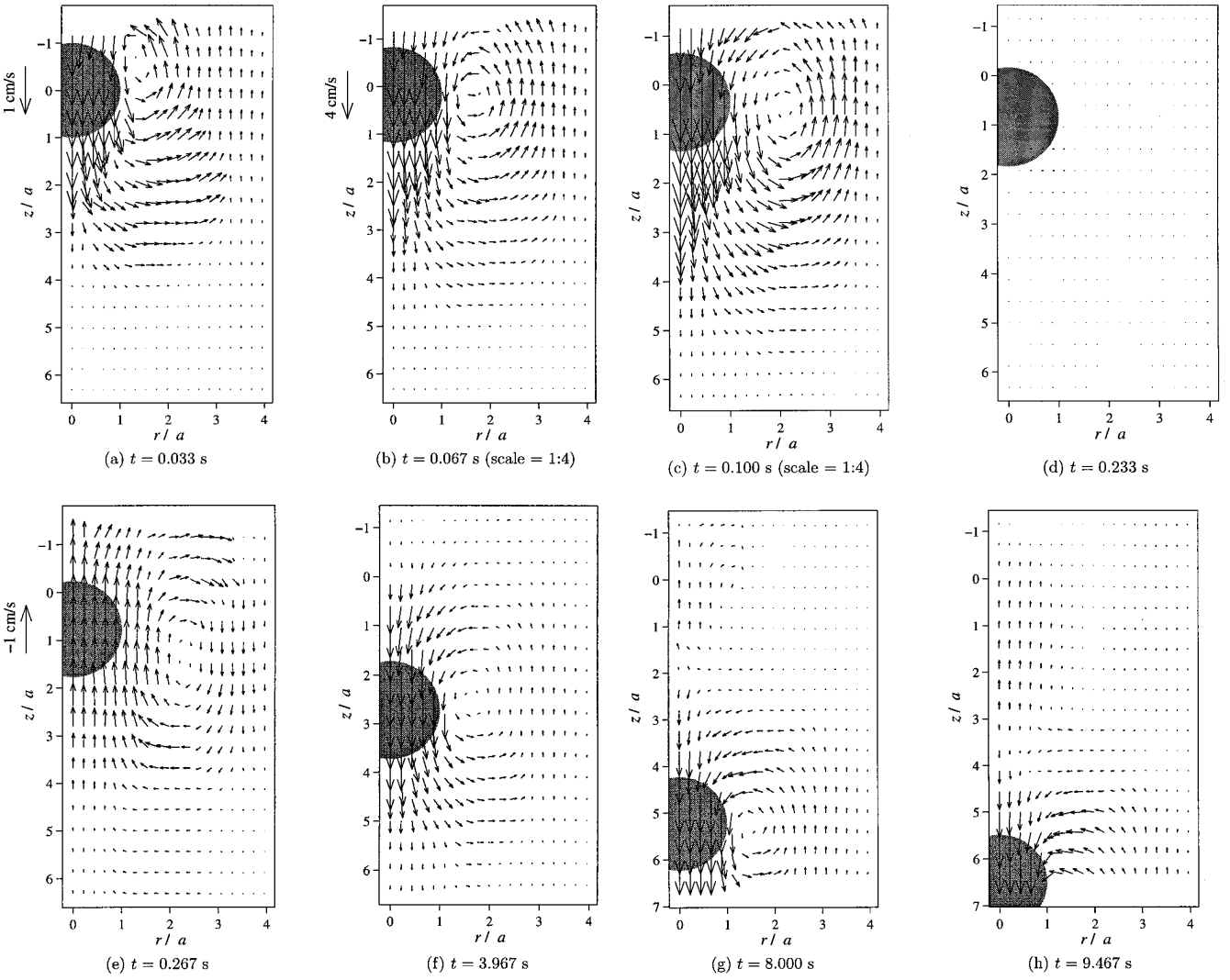

Fig. 13 Full-field DPIV profiles sequencing the transient acceleration of a 1.27 cm radius ceramic sphere from rest at the times indicated: $a/R = 0.243$, $\alpha = 2.45$, $De(\dot{\gamma}) = 2.32$, $Re(\dot{\gamma}) = 0.005$. It is important to note that the magnitude of the velocity vectors in (b) and (c) have been scaled by a factor of 0.25 due to the large velocity overshoot that develops at short times

most constant extensional viscosity in uniaxial elongational flow (as seen in Fig. 3). Subsequently, after the falling sphere passes by a given fluid element, the molecules will relax very quickly because of the absence of a high viscosity solvent and the decrease in the effective relaxation time observed at moderate shear rates. Stress relaxation data for this fluid following cessation of steady shear flow has been presented by Arigo and McKinley (1997). It is this rapid elastic recoil, reminiscent of that observed in an elastic thread, which appears to result in the formation of the negative wake. As the sphere continues to fall, the negative wake grows in strength until the final steady state profile is achieved.

Finally, we point out that in all of the LDV and DPIV experiments, the measured velocities in the wake appear to be stable and the sphere settles at a constant velocity. There was no evidence of a time-dependent flow instability in the negative wake of the type reported by Bisgaard (1983).

Conclusions

Using LDV, we have examined the effects of the density contrast, aspect ratio, and inertia on the development of a negative wake in a viscoelastic shear-thinning fluid. For experiments with similar aspect ratios, the negative wake increases in magnitude with increasing Deborah numbers and is also shifted farther down-

stream. However, the spatial location of the stagnation point where the flow reverses direction remains stationary for a fixed aspect ratio. Nondimensionalizing these results normalizes the upstream velocity as well as the downstream velocity until the point of minimum velocity at z_{min}/a. From this point downstream, there are slight variations in the dimensionless velocity as the wake extends more than 20 radii downstream. Finally, experiments at large Reynolds numbers show that the effect of inertia is to shift the entire wake structure downstream and to reduce the magnitude of the negative wake. This may explain some of the differences in wake profiles observed in fluids with different rheological properties (e.g., Bisgaard, 1983).

Our results provide evidence that the formation of a negative wake is a nonlinear elastic response associated with specific forms of the material functions. Using DPIV to analyze the transient acceleration of a sphere from rest, we see that the negative wake develops from the nonlinear fluid response at large strains long after the transient oscillations associated with linear viscoelasticity and fluid inertia have decayed. Additionally, full-field data from DPIV shows that the largest velocities in the negative wake are concentrated directly behind the sphere in the region of strong extensional flow where the extensional viscosity is large. This wake structure is bounded by a region of high shear at the sphere equator where shear-thinning causes the fluid viscosity to be very low. These competing regions have been considered as one possible mechanism for the formation of the negative wake.

On the basis of large-scale numerical calculations with nonlinear viscoelastic constitutive models, Bush (1994) and Harlen (1997) have both presented criteria that can be used to rationalize the rheological conditions that lead to the development of a negative wake. In simulations with a PTT model, Bush showed that as the dimensionless ratio of the Deborah number (De_0) divided by the Trouton ratio (Tr) became larger, there was an increasing trend for an upstream shift in the streamlines within the wake of the sphere leading to the development of a negative wake. It should be noted that Bush scales the Trouton ratio with the shear-rate–dependent viscosity $\eta(\dot{\gamma})$, and he uses a Deborah number computed using the constant relaxation time λ obtained in the limit of low shear rates; whereas, we use the zero–shear-rate viscosity, η_0, to scale the Trouton ratio and a rate-dependent relaxation time, $\lambda(\dot{\gamma})$, in the Deborah number. These numerical modifications do not affect the generic conclusions obtained by Bush. Consideration of the origins of the terms in $De(\dot{\gamma})$ and Tr shows that this ratio characterizes the relative importance of the normal stress differences in simple shear flow, $N_1=(\tau_{xx}-\tau_{yy})=\Psi_1(\dot{\gamma})\dot{\gamma}^2$, to the normal stress differences in uniaxial extension, $\Delta\tau_{\text{ext}}=(\tau_{zz}-\tau_{rr})=\bar{\eta}(\dot{\varepsilon})\dot{\varepsilon}$. Hence, we consider the normal stress ratio

$$\frac{N_1}{\Delta\tau_{ext}} \sim \frac{(\Psi_1(\dot{\gamma})/2\eta_0)\dot{\gamma}}{\bar{\eta}(\dot{\varepsilon})/\eta_0} \propto \frac{De(\dot{\gamma})}{Tr} \tag{8}$$

where the extensional stress is to be evaluated at a characteristic strain rate $\dot{\varepsilon}=\dot{\gamma}/\sqrt{3}$.

In calculations with the FENE-CR model, Harlen (1997) used the observation that the axial component of the pseudo-body force driving the secondary flow behind the sphere can be expressed as

$$f_z = \frac{\partial \tau_{zz}}{\partial z} + \frac{1}{r}\frac{\partial}{\partial r}(r\tau_{rz}). \tag{9}$$

In conjunction with plots of local dumbbell orientation, Harlen shows that the radial gradients in shear stress and the axial gradients in normal stress counteract each other and drive or retard the formation of a secondary wake. Since the positive tensile stress decays in the wake with decreasing $z\rightarrow-\infty$, the first term in Eq. (9) is positive. The shear stress varies from zero on the centerline and becomes increasingly negative as the radial coordinate increases. Hence the sign of f_z depends on the relative magnitude of each term with $f_z<0$ corresponding to a driving force for a negative wake.

Exact values of the stress gradients in Eq. (9) require numerical simulations; however, we may adopt the arguments of Harlen (1997) by estimating the expected scales of the terms in Eq. (9). In particular, the shear stress will scale with the shear viscosity, $\tau_{rz}\propto\tau_{yx}=\eta(\dot{\gamma})\dot{\gamma}$, while the axial tensile stress will be proportional to the stress difference in uniaxial elongation, $\tau_{zz}\propto\Delta\tau_{ext}$. The DPIV results presented in this article indicate that the radial variations in the flow will scale with the sphere radius a, while the LDV data shows that axial variations occur over a longer length scale proportional to R. Applying these estimates to Eq. (9), we obtain the following condition for the formation of a negative wake

$$\left(\frac{\Delta\tau_{ext}}{\tau_{yx}}\right)\left(\frac{a}{R}\right) = \left(\frac{\bar{\eta}(\dot{\varepsilon})\dot{\varepsilon}}{\eta(\dot{\gamma})\dot{\gamma}}\right)\left(\frac{a}{R}\right) < C \tag{10}$$

where C is a constant whose value depends on the flow kinematics.

While we cannot determine the value of C in Eq. (10), we can compare values of the left-hand side of Eq. (10) for different fluids under similar experimental conditions. We thus compare the shear-thinning, elastic solution employed in the present paper (for which a negative wake is observed) with the constant viscosity, elastic Boger fluid used in previous experiments (Becker et al., 1994; Arigo and McKinley, 1994; Arigo et al., 1995; Rajagopalan et al., 1996) in which an extended wake was found, but no negative wake was seen. The latter fluid consists of 0.31 wt.% polyisobutylene (PIB) dissolved in 4.83 wt.% tetradecane (C14) in a solvent of polybutene (PB) and has been

Table 2 A comparison of the stresses and stress ratios for the PAA test solution and a polyisobutylene (PIB) Boger fluid, used in previous experiments by the authors, at identical Deborah numbers. The values are calculated from the exact solution to the Giesekus model using the multimode parameters listed in Table 1 for the PAA solution and those obtained by Quinzani et al. (1990) for the PIB solution. Note, for comparison, the extensional stresses have been evaluated at a strain rate of $\dot{\varepsilon} = \dot{\gamma}/\sqrt{3}$

	$De(\dot{\gamma})=1.0$		$De(\dot{\gamma})=5.0$	
	PAA	PIB	PAA	PIB
$\dot{\gamma}$ [s^{-1}]	0.061	3.03	9.26	16.5
τ_{yx} [Pa]	8.96	38.7	51.0	207
N_1 [Pa]	17.9	28.3	510	734
$\Delta\tau_{ext}$ [Pa]	62.0	3.60×10^{4}	9.9×10^{3}	3.1×10^{5}
$\Delta\tau_{ext}/\tau_{yx}$	6.92	928	194	1511
$N_1/\Delta\tau_{ext}$	0.289	7.9×10^{-4}	0.051	2.3×10^{-3}

thoroughly characterized in both shear (Quinzani et al., 1990) and extensional flows (Tirtaatmadja and Shidhar, 1993; Spiegelberg et al., 1996). We expect, based on the calculations of Harlen (1997), that smaller values of the stress ratio $\Delta\tau_{ext}/\tau_{yx}$ will indicate the tendency for an upstream shift of the fluid streamlines in the wake and the resultant formation of a negative wake. Table 2 confirms this supposition. Here, the stresses and the stress ratio for the two fluids are listed for two Deborah numbers, $De(\dot{\gamma})=1.0$ and 5.0, which roughly span the range of the experimental results. For both Deborah numbers, the extreme extensional-thickening in the PIB fluid leads to large extensional stresses in the wake of the sphere that greatly dominate the shear stresses. This gives rise to a very large stress ratio, much greater than that in the PAA fluid where the steady extensional viscosity remains small and approximately constant for all strain rates (see Fig. 2).

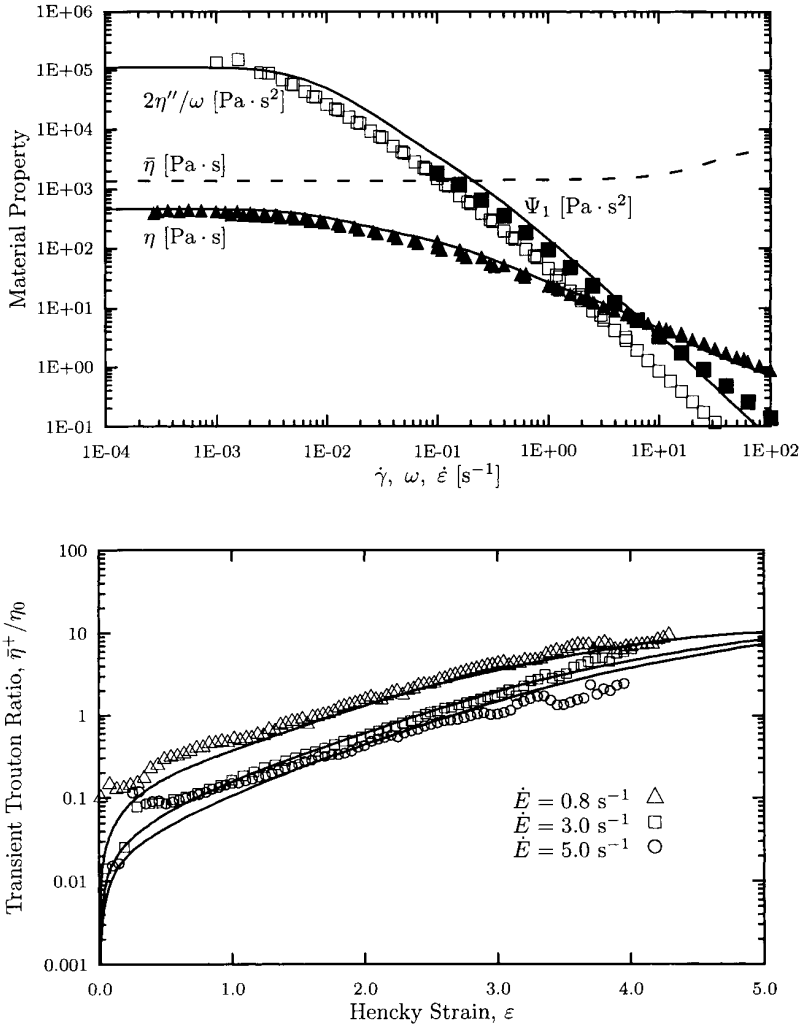

Fig. A1 (a) The steady shear and extensional rheological properties and (b) the transient uniaxial extensional response of the shear-thinning, viscoelastic test fluid. The curves are the predictions of the four-mode PTT model using the parameters specified in Table 1

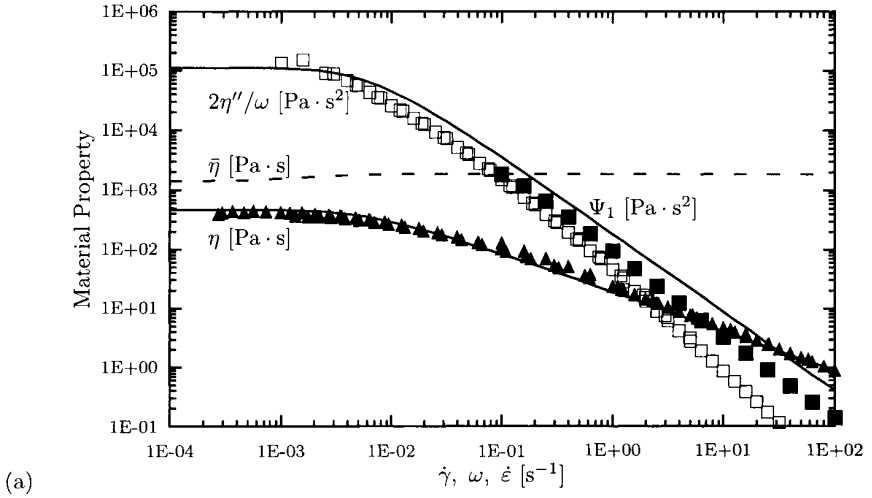

(a)

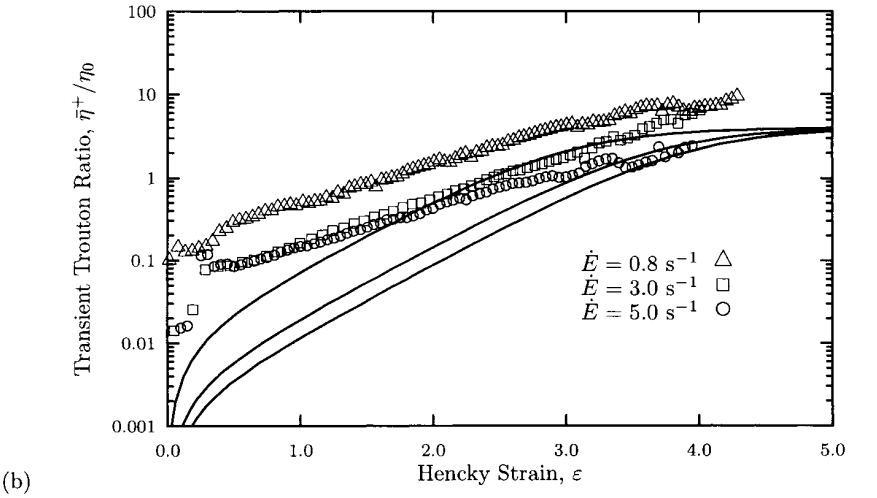

(b)

Fig. A2 (a) The steady shear and extensional rheological properties and (b) the transient uniaxial extensional response of the shear-thinning, viscoelastic test fluid. The curves are the predictions of the single-mode, modified PTT model using the parameters $\eta_0 = 464$ Pa·s, $\lambda = 121$ s, $\varepsilon = 0.5$, and $\xi = 0$

Additionally, Table 2 lists the values of the normal stress ratio, $N_1/\Delta\tau_{ext}$, as proposed by Bush (1994). The trends here also confirm Bush's observations that increasing this ratio leads to a tendency for the formation of a negative wake. Hence, it is not possible to differentiate between which mechanism is primarily responsible for the formation of the negative wake, only that it is a very sensitive function of the nonlinear rheology of the test fluid. In practice, the difference between the two criteria is unimportant since for many polymeric fluids it is found experimentally that the first normal stress difference is directly related to the shear stress through a relationship of the form $N_1 = A\tau_{yx}^b$ with $b \approx 2$ (Barnes et al., 1989). Hence, if the criterion proposed by Bush is valid, then the condition suggested by Harlen will also be valid. In either case, the key factor is the value of the extensional stress that develops in the wake of the sphere. The experimental fluids used by Sigli and Countanceau (1977), by Bisgaard (1983), and by Maalouf and Sigli (1984) were all concentrated aqueous polymer solutions that may be expected to exhibit very similar extensional stress growth characteristics to the present fluid.

Finally, we note that in all of the experiments performed in conjunction with this paper (not just those presented here) the flow appeared to be stable within the wake. No instabilities of the type described by Bisgaard (1983) were seen.

Acknowledgements The authors would like to acknowledge the support of the National Science Foundation under grant No. CTS9553216 and helpful discussions with Dr. Oliver Harlen. Additional thanks goes to Dr. Stephen Spiegelberg of Cambridge Polymer Group, Inc. for providing the extensional viscosity measurements and Dr. Peyman Pakdel for his help with DPIV.

Appendix

Figs. A1 and A2 are provided for completeness. Here, the Phan-Thien–Tanner constitutive model has been

used to fit the rheological data for the PAA test fluid. The PTT constitutive model is ideal in that it provides two adjustable material parameters, ξ and ε, which isolate the non-linear shear and extensional effects, respectively. In Fig. A1, the viscometric properties and the transient extensional viscosity are fitted using a four-mode formulation of the PTT model with the linear form of the network function, i.e., $f(\mathrm{tr}\,\tau_p)=1+\varepsilon\,\mathrm{tr}\,\tau_p$. As with the Giesekus fit in Fig. 2, the same linear viscoelastic spectrum of viscosities, η_j, and relaxation times, λ_j, are used, and the PTT parameters ξ_j and ε_j are chosen to provide the best fit to both the shear and extensional flows. For simplicity, single values for $\xi_j=0.1$ and $\varepsilon_j=0.15$ are chosen for all four modes as listed in Table 1. The shear rheology is shown in Fig. A1a. The PTT model provides an excellent fit to the viscosity; however, the model slightly overpredicts the normal stress coefficient at low shear rates and underpredicts it at high shear rates. The PTT model also predicts a much greater extensional-thickening effect in steady extensional flow at high strain rates than does the Giesekus model. The transient Trouton ratio is shown in Fig. A1b. The multimode PTT model provides a much better fit to the measured data for all three strain rates than the Giesekus model did, due to the flexibility of freely adjusting the parameter ε_j.

Most numerical calculations are performed with single-mode viscoelastic constitutive equations, and it is illustrative to consider how well such models accurately capture the material functions of the test fluid. In Fig. A2, the viscometric properties have been fitted to a single-mode, modified PTT model with $\xi=0$. In this case, the constitutive model parameters are the zero–shear-rate viscosity $\eta_0=464$ Pa·s, the "average" relaxation timescale estimated from $\Psi_{10}/2\eta_0\simeq\lambda=121$ s, and the PTT parameter $\varepsilon=0.5$. While this model provides a good fit to the steady shear data shown in Fig. A2b, the comparisons with the transient uniaxial extension experiments point out, once again, the intrinsic limitations of single-mode constitutive models, particularly at short timescales that simply cannot be captured by the long relaxation time associated with this fluid. In an Eulerian-steady complex flow such as the motion past a sphere settling at a steady velocity, such a response will result in an unrealistic rate of stress growth as fluid elements are convected past the sphere.

References

Acharya A, Mashelkar RA, Ulbrecht J (1976) Flow of inelastic and viscoelastic fluids past a sphere. Part II: Anomalous separation in the viscoelastic fluid flow. Rheol Acta 15:471–478

Agarwal US, Dutta A, Mashelkar RA (1994) Migration of macromolecules under flow: The physical origin and engineering applications. Chem Eng Sci 49:1693–1717

Arigo MT, McKinley GH (1994) The steady and transient motion of a sphere through a viscoelastic fluid. ASME Fluids Engineering Division, 29th Forum on Cavitation and Multiphase-Flow 194:139–147

Arigo MT, McKinley GH (1997) The effects of viscoelasticity on the transient motion of a sphere in a shear-thinning fluid. J Rheol 41:103–128

Arigo MT, Rajagopalan D, Shapley N, McKinley GH (1995) The sedimentation of a sphere through an elastic fluid. Part 1: Steady motion. J Non-Newtonian Fluid Mech 60:225–257

Barnes HA, Hutton JF, Walters K (1989) An introduction to rheology. Elsevier, New York

Becker LE, McKinley GH, Rasmussen HK, Hassager O (1994) The unsteady motion of a sphere in a viscoelastic fluid. J Rheol 38:377–403

Becker LE, McKinley GH, Stone HA (1996) Sedimentation of a sphere near a plane wall: Weak non-Newtonian and inertial effects. J Non-Newtonian Fluid Mech 63:201–233

Bisgaard C (1983) Velocity fields around spheres and bubbles investigated by laser-Doppler anemometry. J Non-Newtonian Fluid Mech 12:283–302

Bush MB (1993) The stagnation flow behind a sphere. J Non-Newtonian Fluid Mech 49:103–122

Bush MB (1994) On the stagnation flow behind a sphere in a shear-thinning viscoelastic fluid. J Non-Newtonian Fluid Mech 55:229–247

Chhabra RP (1992) Bubbles, drops, and particles in non-Newtonian fluids. CRC Press, Boca Raton

Harlen OG (1997) The negative wake behind a sedimenting sphere. (In preparation)

Harlen OG, Rallison JM, Szabo P (1995) A split Lagrangian-Eulerian method for simulating transient viscoelastic flows. J Non-Newtonian Fluid Mech 60:81–104

Hassager O (1979) Negative wake behind bubbles in non-Newtonian liquids. Nature 29:402–403

Hassager O (1988) Working group on numerical techniques. J Non-Newtonian Fluid Mech 29:2–5

Jin H, Phan-Thien N, Tanner RI (1991) A finite element analysis of the flow past a sphere in a cylindrical tube: PTT fluid model. Comp Mech 8:409–422

Kolte MI, Rasmussen HK, Hassager O (1997) Transient filament stretching rheometer II: Numerical simulation. Rheol Acta 36:285–302

Maalouf A, Sigli D (1984) Effects of body shape and viscoelasticity on the slow flow around an obstacle. Rheol Acta 23:497–507

Pakdel P, McKinley GH (1997) Digital particle imaging velocimetry of viscoelastic fluids. AIChEJ 43:289–302

Quinzani LM, McKinley GH, Brown RA, Armstrong RC (1990) Modeling the rheology of polyisobutylene solutions. J Rheol 34:705–748

Rajagopalan D, Arigo MT, McKinley GH (1996) The sedimentation of a sphere through an elastic fluid. Part 2: Transient motion. J Non-Newtonian Fluid Mech 65:17–46

Satrape JV, Crochet MJ (1994) Numerical simulation of the motion of a sphere in a Boger fluid. J Non-Newtonian Fluid Mech 55:91–111

Sigli D, Coutanceau M (1977) Effect of finite boundaries on the slow laminar isothermal flow of a viscoelastic fluid around a spherical obstacle. J Non-Newtonian Fluid Mech 2:1–21

Spiegelberg SH, Ables DC, McKinley GH (1996) The role of end-effects on measurements of extensional viscosity in filament stretching rheometers. J Non-Newtonian Fluid Mech 64:229–267

Tavener SJ (1994) Stability of the O(2)-symmetric flow past a sphere in a pipe. J Fluid Mech 6:3884–3892

Tirtaatmadja V, Shidhar T (1993) A filament stretching device for measurement of extensional viscosity. J Rheol 37:1081–1102

Van Dyke M (1982) An album of fluid motion. Parabolic Press, Stanford

Walters K, Tanner RI (1992) The motion of a sphere through an elastic fluid. In: Chhabra RP, DeKee D (eds) Transport processes in bubbles, drops and particles. Hemisphere, New York, pp 73–86

White SA, Baird DG (1996) The importance of extensional flow properties on planar entry flow patterns of polymer melts. J Non-Newtonian Fluid Mech 20:93–101

Yao M, Spiegelberg SH, McKinley GH (1998) Fluid dynamics of weakly strain-hardening fluids in a filament stretching device. J Non-Newtonian Fluid Mech, in press

Zheng R, Phan-Thien N, Tanner RI (1991) The flow past a sphere in a cylindrical tube: effects of inertia, shear-thinning and elasticity. Rheol Acta 30:499–510